Advances in
Geo-Energy Research

Vol. 19, No. 2, p. 131-145, 2026

Original article

Impact of energized pre-fracturing on fracture network evolution and imbibition in tight oil reservoirs

Hongyan Qu[1]*, Mengyao Wu[2], Jiayue Gan[1], Yan Peng[3], Fujian Zhou[1], Zhongwei Chen[4]

[1]*National Key Laboratory of Petroleum Resources and Engineering, China University of Petroleum, Beijing 102249, P. R. China*
[2]*PetroChina Tarim Oilfield Company, Korla 841000, P. R. China*
[3]*College of Petroleum, China University of Petroleum-Beijing at Karamay, Karamay 834000, P. R. China*
[4]*School of Mechanical and Mining Engineering, The University of Queensland, St Lucia QLD 4072, Australia*

Keywords:
Energized pre-fracturing
tight conglomerate reservoir
supercritical CO_2
fracture propagation
imbibition enhanced oil recovery

Cited as:
Qu, H., Wu, M., Gan, J., Peng, Y., Zhou, F., Chen, Z. Impact of energized pre-fracturing on fracture network evolution and imbibition in tight oil reservoirs. Advances in Geo-Energy Research, 2026, 19(2): 131-145.
https://doi.org/10.46690/ager.2026.02.03

Abstract:
Energized pre-fracturing has emerged as an effective approach for enhancing reservoir energy, fracture complexity and oil recovery in tight reservoirs. However, the mechanisms by which fracture propagation induced by different energized pre-pad fluids governs subsequent imbibition-driven oil recovery remain insufficiently understood. To address this issue, an integrated experimental framework was established to investigate the coupled evolution of fracture networks and pore-scale oil displacement during energized pre-fracturing. By combining X-ray computed tomography for quantitative fracture characterization and dynamic nuclear magnetic resonance for monitoring imbibition-driven oil recovery, the interactions between fracture-scale architecture and pore-scale fluid redistribution were systematically elucidated. The results demonstrate that, compared to conventional fracturing, energized pre-fracturing not only lowers breakdown pressure but also promotes the formation of more complex, highly connected fracture networks, which in turn substantially enhance ultimate oil recovery. Notably, gaseous pre-pad fluids exhibit clear advantages over aqueous systems, with supercritical CO_2 generating the lowest breakdown pressure and the most intricate multi-branch fracture networks, as indicated by higher fracture fractal dimension and area ratio. These fracture characteristics significantly facilitate imbibition efficiency, resulting in higher oil recovery. Pore-scale analysis further reveals that oil mobilization is dominated by contributions from micropores and mesopores, underscoring the critical role of energized pre-fracturing in activating oil stored in small-scale pore systems. The proposed multi-scale methodology, integrating fluid properties, fracture network evolution, and imbibition dynamics, provides a mechanistic basis and practical guidance for optimizing energized fracturing and improving the efficient development of tight conglomerate reservoirs.

1. Introduction

Tight conglomerate reservoirs, characterized by high gravel content, constrained hydrocarbon storage capacity and extremely low permeability (Nelson, 2009; Sondergeld et al., 2010; Kozhevnikov et al., 2024), constitute an important unconventional resource base in major basins in China, such as the Mahu Sag in the Junggar Basin, the Kuqa Depression in the Tarim Basin, the Xujiaweizi region in the Daqing Oilfield, and the Jiyang and Dongying sags in the Shengli Oilfield (Clarke, 1979). Despite their considerable resource potential, the economic development of these challenging reservoirs necessitates effective stimulation, with hydraulic fracturing serving as the primary technique (Hubbert and

Yandy
Scientific
Press

---

*Corresponding author.
E-mail address: hongyan.qu@cup.edu.cn (H. Qu); wmy050626@163.com (M. Wu); 15893429758@163.com (J. Gan); yan.peng@cup.edu.cn (Y. Peng); zhoufj@cup.edu.cn (F. Zhou); zhongwei.chen@uq.edu.au (Z. Chen).

Received November 16, 2025; revised December 19, 2025; accepted January 10, 2026; available online January 14, 2026.

Willis, 1957; Goral et al., 2020). However, post-fracturing production in such reservoirs often experiences rapid decline, yielding suboptimal primary recovery.

To overcome this limitation, energized pre-fracturing, where specific fluids were injected as a pre-pad prior to the main fracturing, has been increasingly adopted to enhance reservoir energy, promote fracture complexity, and ultimately improve oil recovery. Depending on their physical state, energized pre-pad fluids can be broadly classified into aqueous systems (e.g., fresh water, produced water, and flowback fluid) and gaseous/supercritical systems (e.g., CO_2 and N_2). They are typically injected at low pumping rates before the primary fracturing fluid to elevate formation pressure and weaken the mechanical strength of the reservoir rock (Faroughi and Pruvot, 2018; Lei et al., 2020; Fang et al., 2023; Sun et al., 2025), after which water-based fracturing fluids, such as slickwater, are introduced to generate fracture networks.

The selection of pre-pad fluids involves critical trade-offs between operational feasibility and stimulation effectiveness. Aqueous fluids are generally cost-effective but are often associated with large water consumption and potential formation damage (Qu et al., 2023c; Holditch, 1979; Bahrami et al., 2012; Soomro et al., 2025). The reuse of minimally treated produced water or flowback fluid can partially alleviate freshwater demand and wastewater disposal costs (Rodriguez et al., 2020; Middleton et al., 2015). In contrast, gaseous and supercritical (SC) fluids, particularly supercritical CO_2 (SC-CO_2) exhibit superior compressibility and injectivity (Perera et al., 2011), making them especially attractive for low-pressure or water-sensitive formations, while also offering the added benefit of geological CO_2 sequestration (Mojid et al., 2021; Ampomah et al., 2017; Ishida et al., 2012; Tang et al., 2025). Nevertheless, operational risks such as gas channelling and early breakthrough must be carefully considered (Huang et al., 2020; Elgibaly et al., 2021; Qin et al., 2022).

The effectiveness of energized pre-fracturing arises from a series of coupled mechanisms, including pore pressure enhancement that reduces effective stress, activation of natural fractures that lowers breakdown pressure (Zhang et al., 2025), and physicochemical interactions between fluids and rock that weaken the rock matrix (Qu et al., 2023a, 2023b; Xie et al., 2025; Dai et al., 2025). These processes collectively indicate that energization, fracture propagation, and subsequent oil displacement are intrinsically interrelated rather than independent phenomena.

Despite this understanding, a pronounced gap remains between the integrated nature of field-scale energized pre-fracturing and existing laboratory-scale experimental approaches. Common laboratory studies decouple these processes by simulating energization through static pressurization or soaking (Cipolla et al., 2010), rather than dynamic fluid injection, thereby separating it from the subsequent fracturing and imbibition. Although true triaxial systems are effective for investigating fracture propagation under *in situ* stress conditions (Warpinski et al., 2009; Kamali and Ghassemi, 2022; Yu et al., 2024; Li et al., 2025), they are incompatible with the cylindrical core geometries required for nuclear magnetic resonance (NMR) monitoring of imbibition (Hosseini et al., 2024). Consequently, the interlinked processes of energization, fracture propagation and imbibition-driven oil recovery are typically investigated in isolation.

This disconnect is particularly problematic because pressure elevation and fracture propagation directly govern subsequent fluid imbibition and oil displacement during the well shut-in period (Li et al., 2025). Conventional recovery evaluation methods based on volumetric or gravimetric measurements lack the resolution needed to capture complex fracture-matrix interactions (Morrow and Mason, 2001; Hamida and Babadagli, 2007; Peng et al., 2019; Xu et al., 2021). In contrast, advanced techniques such as NMR, especially when integrated with mercury injection porosimetry (MIP) analysis, enable precise visualization and quantitative characterization of fluid distribution and mobilization across the full pore-size spectrum (Alharthy et al., 2018; Zhang et al., 2024; Wang et al., 2025; Zhao et al., 2025).

Accordingly, the integrated mechanisms linking pre-pad fluid type, fracture network evolution and imbibition-driven oil recovery in tight conglomerate reservoirs remain insufficiently understood. The superimposed physicochemical interactions among pre-pad fluids, fracturing fluids, reservoir oil and rock further complicate the prediction of stimulation performance.

To bridge this gap, this study proposes an integrated experimental methodology that seamlessly couples energized pre-fracturing with imbibition-driven oil displacement. Using tight conglomerate samples from the Xinjiang Oilfield and a self-developed equipment system, the performance of aqueous and gaseous/SC pre-pad fluids was systematically evaluated. Fracture propagation was quantitatively characterized by X-ray computed tomography (CT), while oil displacement dynamics were resolved using NMR. This multi-scale approach elucidates the coupled mechanisms underlying production enhancement through energized pre-fracturing and provides a scientific basis for optimizing stimulation strategies in tight conglomerate reservoirs.

2. Experimental methodology

2.1 Sample and fluid preparation

2.1.1 Rock samples

Tight conglomerate cores collected from the Lower Urho Formation in the Xinjiang Oilfield served as the experimental samples in this study. To minimize bias caused by strong lithological heterogeneity, multiple full-diameter cores with consistent drilling orientation and comparable petrophysical properties were first screened. Each candidate core was then examined by X-ray CT to document the initial internal structure and exclude specimens containing large natural fractures or severe gravel segregation. This screening ensured that the observed responses were representative of the rock fabric rather than dominated by local defects.

Nine qualified specimens were prepared for energized pre-fracturing and machined into standard cylinders (38 mm in diameter and 57 mm in height). An axial borehole (8 mm in diameter and 30 mm in depth) was drilled to mimic the wellbore (Fig. 1(a)). To enable NMR measurements without magnetic

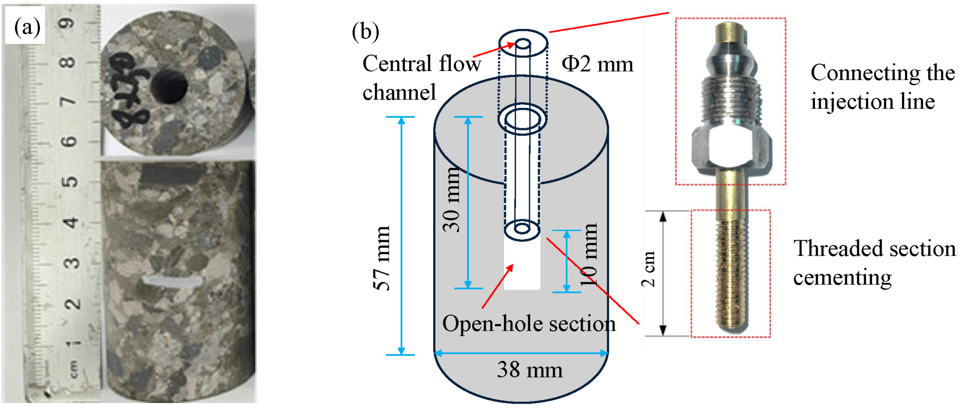

Fig. 1. Schematic diagrams of well completion and rock samples: (a) Prepared rock specimens and (b) well completion and copper wellbore assembly.

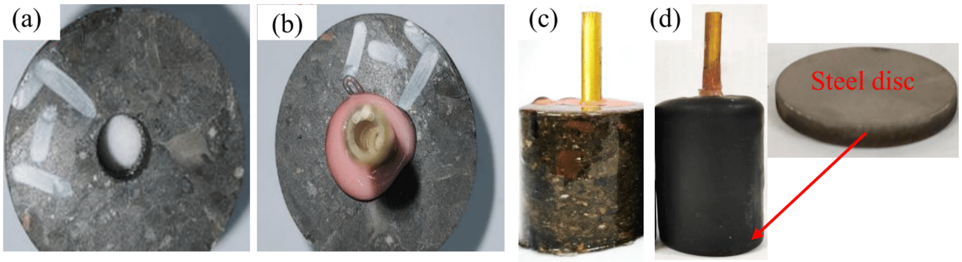

Fig. 2. Well cementing of rock samples: (a) Sand-filling of the open-hole, (b) wellbore cementing, (c) rock sample sealing, and (d) wrapping with heat-shrink tubing.

interference, a custom copper wellbore was cemented into the borehole using epoxy resin. The assembly comprises a central flow channel (2 mm in diameter) and a 10 mm open-hole section at the bottom for fluid injection, as shown in Fig. 1(b). Sand packing was applied to isolate the open-hole interval. After completion, each specimen was sealed with an organic potting compound, wrapped with heat-shrink tubing, reinforced with epoxy resin, and end-constrained using steel plates to improve confinement and prevent leakage during pre-fracturing. The detailed preparation workflow is illustrated in Fig. 2.

Prior to saturation, all specimens were oven-dried at 102 °C for 48 h until constant mass was achieved (mass change $\leq$ 0.1% over 24 h). CT scans of the dried samples were performed to confirm gravel distribution and identify natural fractures. The samples were subsequently vacuum-saturated with synthetic oil under reservoir temperature and pressure conditions (75 °C and 24 MPa) and aged for 7 days. Final oil saturation was verified by NMR once the sample mass stabilized.

2.1.2 Synthetic oil and pre-fracturing fluid

To reproduce the viscosity of reservoir oil, filtered field oil was blended with kerosene at a volumetric ratio of 1:3, yielding a viscosity of 1.15 mPa·s. Two aqueous pre-pad fluids (purified fresh water and produced water from the Xinjiang Oilfield) and two gaseous pre-pad fluids (CO_2 and N_2, 99.9% purity) were employed. Under the target reservoir conditions (75 °C and 24 MPa), CO_2 exists in the supercritical state.

Table 1. Physical property of the pre-fracturing fluids employed in the experiments.

Pre-pad Fluid	P (MPa)	T (°C)	ρ (g/cm^3)	μ (mPa·s)	γ (mN/m)
Produced water	0.1	20	1.089	1.1	23.75
Fresh water	0.1	20	1.000	1.00	17.56
Water	7.5-24	75	0.98-0.99	0.38	/
SC-CO_2	7.5-24	75	0.02-0.72	0.02-0.06	/
N_2	7.5-24	75	0-0.22	0.02-0.03	/

According to field data, the produced water is a $NaHCO_3$-type brine with a density of 1.089 g/cm^3, a viscosity of 1.1 mPa·s, and an interfacial tension of 23.75 mN/m at ambient conditions, compared with 1.00 g/cm^3, 1.00 mPa·s, and 17.56 mN/m for fresh water. The density and viscosity of the pre-pad fluids under reservoir conditions were compiled from the literature (Table 1).

Slickwater (20 mPa·s) was used as the primary fracturing fluid. To suppress hydrogen signals from aqueous fluids during NMR measurements, 15 wt% $MnCl_2$ was added to all aqueous fluids (both aqueous pre-pads and slickwater), ensuring that the detected NMR signals originated predominantly from oil.

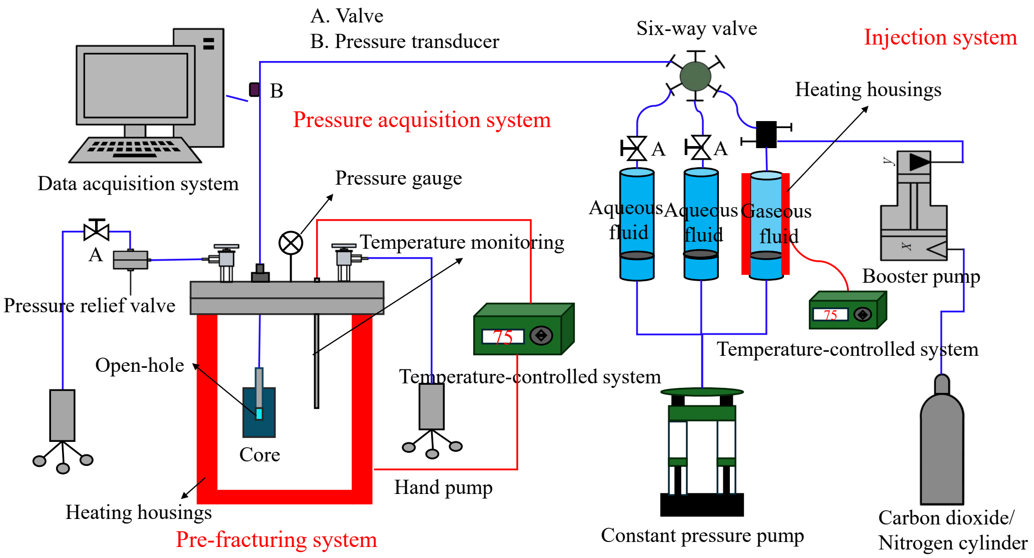

Fig. 3. Schematic of the pseudo-triaxial energized pre-fracturing simulation system.

2.2 Experimental setup

2.2.1 Energized pre-fracturing system

A custom-built pseudo-triaxial energized pre-fracturing system was developed to accommodate both aqueous and gaseous pre-pad fluids and to capture fracture initiation/propagation under controlled conditions. The system integrates three sub-modules, including fluid storage and injection, pseudo-triaxial pre-fracturing, and pressure monitoring and data acquisition, as illustrated in Fig. 3.

The injection unit includes three parallel heated intermediate cylinders (2,000 mL each), for gaseous pre-pad fluid, aqueous pre-pad fluid, and slickwater, respectively. Gaseous fluids supplied from gas cylinders were pressurized via a booster pump, and all fluids were delivered by an ISCO pump (maximum rate: 60 mL/min). The specimen was mounted in a pressure vessel where confining pressure (up to 18 MPa) was applied to represent the *in-situ* stress. In addition, a backpressure line was incorporated to enhance operational safety. Injection pressure was recorded in real time using a high-precision pressure transducer (±0.01 MPa).

2.2.2 Characterization and imaging techniques

Multi-scale characterization of fracture networks and fluid distribution relied on complementary imaging and analytical techniques. A GE Brivo CT385 scanner was employed to image fracture networks before and after pre-fracturing and after imbibition. Scans were performed at 140 kV and 160 mA with a slice thickness of 0.625 mm. A Niuman MacroMR12-150H-I low-field NMR system was used to quantify fluid saturation and pore-scale redistribution. T_2 spectra (echo time: 0.2 ms; echoes: 18,000) were acquired at key stages (after oil saturation, after pre-fracturing and during/after imbibition).

2.3 Experimental procedure

This study evaluates energized pre-fracturing using aqueous (fresh water and produced water) and gaseous (N_2 and SC-CO_2) pre-pad fluids, with a focus on both fracture propagation and imbibition-driven oil recovery. All experiments were conducted at 75 °C, consistent with the reservoir temperature and within system operational limits. The workflow comprises two coupled stages.

In the first stage of energized pre-fracturing, pre-pad fluid was injected into the oil-saturated specimen until a target bottom-hole pressure was reached while remaining below the confining pressure (12 MPa) to maintain confinement integrity. To establish a consistent energization benchmark across fluids with markedly different compressibility, a pressure-equivalent (rather than volume-equivalent) criterion was adopted (Bennion and Bachu, 2008). For gaseous tests, the initial injection pressure was set to 7.5 MPa to maintain CO_2 in the supercritical state. Since aqueous fluids are far less compressible, the injection rate was reduced relative to gaseous fluids. Slickwater injection for fracturing was then performed at 50 mL/min. Throughout the process, downhole pressure was monitored continuously to quantify energization capacity and determine breakdown pressure. Fracture complexity was subsequently evaluated from CT images by calculating fracture fractal dimension and fracture area ratio using the quantitative method described in Section 2.4.1.

After pre-fracturing, the fractured rock samples underwent a well shut-in to simulate post-fracturing pressurized imbibition. All imbibition tests were conducted consistently at 75 °C and 24 MPa for 120 h. NMR T_2 spectra were analyzed to quantify pore-scale fluid redistribution and the corresponding oil recovery efficiency induced by imbibition under different pre-pad fluid conditions.

To ensure repeatability, duplicate tests were performed for each pre-pad fluid. A representative subset of samples was selected for detailed analysis of fracture propagation, fluid distribution and oil recovery. Experimental conditions are summarized in Table 2.

Table 2. Experimental design and injection rates for energized pre-fracturing and imbibition.

No.	Pre-pad fluid	Pre-fracturing injection rate (mL/min)
0	None	0
1, 5	Fresh water	2
2, 6	Produced water	2
3, 7	SC-CO_2	20
4, 8	N_2	20

2.4 Quantitative evaluation methods

2.4.1 Fracture characterization via CT

CT images were segmented and reconstructed in AVIZO to obtain three-dimensional (3D) fracture networks, which were then quantified using fractal analysis, a widely adopted approach for describing complex fracture-pore systems in heterogeneous media. Fracture complexity was evaluated using two metrics including fractal dimension (FD) and fracture area ratio (AR). These metrics capture tortuosity arising from gravel obstruction (e.g., bypassing or penetrating) without explicitly modelling individual gravel particles.

1) Fractal dimension

The fractal dimension (D_f) was calculated using the box-counting method (Mandelbrot, 1982; Xie, 1993; Saidian and Prasad, 2015). Briefly, the 3D fracture pattern is overlaid with cubic grids of side length, l, and the number of cubes, $N(l)$, intersecting fractures is counted. Repeating the procedure while reducing l yields a power-law relationship between $N(l)$ and l (Mandelbrot, 1982; Xie, 1993):

$$N(l) \propto l^{-D_f} \tag{1}$$

where D_f is the fractal dimension, $N(l)$ represents the number of fracture-containing cubes with l as the length of one side of the small cube.

Taking the natural logarithm on both sides yields the linear form as follows:

$$\ln N(l) = -D_f \ln l + C \tag{2}$$

where C is constant.

The fractal dimension D_f is therefore determined as the negative slope of the linear regression between $\ln N(l)$ and $\ln l$:

$$D_f = -\frac{\mathrm{d}\ln N(l)}{\mathrm{d}\ln l} \tag{3}$$

A higher D_f value indicates a more complex and space-filling fracture network.

2) Fracture surface area and area ratio

Fracture surface area S_f is a critical parameter for evaluating stimulation effectiveness. It is computed from segmented fracture-surface voxels as follows (Vogel and Kretzschmar, 1996):

$$S_f = N_f s^2 \tag{4}$$

where N_f is the number of voxels on the fracture surface, and s denotes the voxel size (200 μm), namely the image resolution.

The fracture area ratio is defined as the ratio of the true 3D fracture surface area (S_f) to its two-dimensional (2D) orthographic projection area (S_p) on the transverse plane as follows:

$$R_a = \frac{S_f}{S_p} \tag{5}$$

where R_a is the fracture area ratio, S_p equals the cross-sectional area of the cylindrical sample minus the borehole area.

2.4.2 Pore-scale analysis by integrating NMR and MIP

NMR provides a non-destructive means of tracking pore-scale fluid distribution by detecting hydrogen-bearing fluids within the pore space, with the transverse relaxation time (T_2) spectrum reflecting pore-size-dependent relaxation behavior. In this study, Mn^{2+} (from $MnCl_2$) suppressed hydrogen signals from aqueous phases, so that changes in the measured NMR signal primarily reflected oil redistribution.

Signals were acquired using the Carr-Purcell-Meiboom-Gill pulse sequence. The total transverse relaxation rate for fluid in porous media is expressed as follows (Abragam, 1961):

$$\frac{1}{T_{2,total}} = \frac{1}{T_{2,S}} + \frac{1}{T_{2,D}} + \frac{1}{T_{2,B}} \tag{6}$$

where T_2 is the transverse relaxation time, $T_{2,total}$ is the total transverse relaxation time, $T_{2,s}$ is the surface relaxation time, $T_{2,B}$ is the bulk relaxation time, and $T_{2,D}$ is the diffusion relaxation time.

For the oil-water system considered here, the bulk and diffusion relaxations are typically much slower than surface relaxation, allowing T_2 to be approximated by the surface relaxation term, which is further related to the transversal surface relaxivity (ρ_2) and the specific surface area of the pore (S/V) as follows (Brown and Fatt, 1956):

$$\frac{1}{T_2} \approx \frac{1}{T_{2,S}} = \rho_2 \left(\frac{S}{V}\right)_{pore} \tag{7}$$

where S/V is the pore-specific surface area, defined as the ratio of the pore surface area of the rock (S) to the pore volume (V), and can be calculated through the value of F_s/r_c^n.

F_s denotes the geometric factor ($F_s = 3$ for spherical pore; $F_s = 2$ for columnar pore), and r_c is the pore radius.

The above equation can be rewritten as:

$$T_2 \approx \frac{r_c^n}{\rho_2 F_s} \tag{8}$$

$$M = \sqrt[n]{\rho_2 F_s} \tag{9}$$

The conversion from T_2 to pore radius distribution can be calibrated using high-pressure MIP data and converted via established correlations (Coates et al., 1999):

$$r_c \approx M \sqrt[n]{T_2} \tag{10}$$

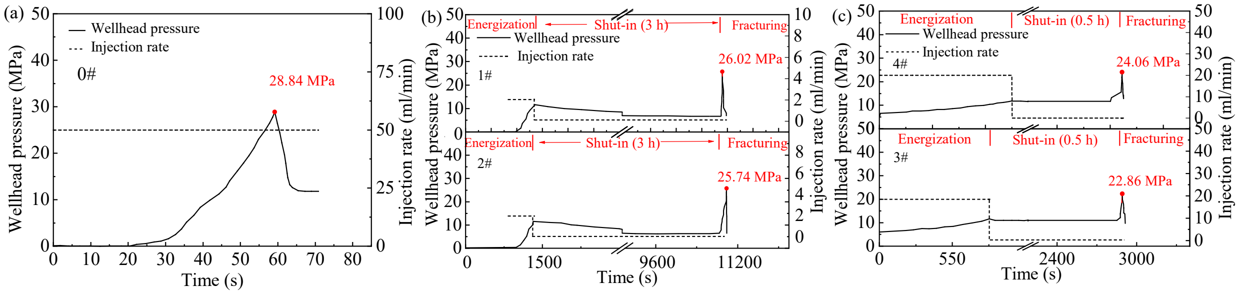

Fig. 4. Evolution of injection pressure during energized pre-fracturing under different treatment schemes: (a) Conventional slickwater fracturing without pre-pad injection, (b) with aqueous pre-pad fluids and (c) with gaseous pre-pad fluids.

Table 3. Representative outcomes of energized pre-fracturing with different pre-pad fluids.

Energized pre-pads	Breakdown pressure (MPa)	Fracture pattern and morphology
/	28.89	One main fracture
Fresh water	26.02	One main fracture
Produced water	25.74	One main fracture
SC-CO_2	22.86	Contains branching fractures
N_2	24.06	Contains branching fractures

where M and n are the NMR conversion coefficients, which can be calculated and calibrated by integrating the experimental data of MIP. The resulting pore-radius mapping was further refined by integrating mercury intrusion capillary pressure and nitrogen adsorption data through interpolation (Qu et al., 2024).

2.4.3 Calculation of oil recovery efficiency

Based on the calibrated T_2-pore radius relationship, NMR was employed to quantify the content of hydrogen-bearing substance (simulated oil) and its redistribution across different pore-size ranges, thereby enabling the calculation of oil recovery efficiency.

The cumulative NMR signal intensity within a given pore-size interval is proportional to the corresponding oil volume (Coates et al., 1999):

$$A=\int_{r_1}^{r_2} Y \mathrm{d}r \tag{11}$$

where A denotes the cumulative signal intensity, r is the pore radius, r_1 is the initial pore radius, r_2 is the terminal pore radius, and Y is the signal amplitude.

The oil recovery efficiency (η_0) at any stage (i) are calculated from the change in the total NMR signal area as follows:

$$\eta_0=\frac{A_0-A_i}{A_0}\times 100\% \tag{12}$$

In addition, the contribution of each pore-size range j to the total recovered oil is quantified as follows:

$$b=\frac{A_{0j}-A_{ij}}{A_0-A_i}\times 100\% \tag{13}$$

where b is the contribution ratio, A_0 represents the NMR signal intensity when the sample is saturated with oil, A_i is the NMR signal intensity of the sample at time i, A_{0j} and A_{ij} are the NMR signal intensities of the oil-saturated sample and of the sample at time i within a specific pore-throat size range j (e.g., small, medium, or large pores as defined by T_2), respectively.

3. Results and discussion

In this section, the fracture propagation and oil recovery responses during energized pre-fracturing using aqueous pre-pad fluids (fresh water and produced water) and gaseous/SC pre-pad fluids (SC-CO_2 and N_2) were compared. To ensure a consistent baseline across treatments, slickwater was used as the main fracturing fluid in all cases. Given the strong heterogeneity of conglomerates (e.g., uneven gravel distribution and pre-existing microcracks), representative samples exhibiting the highest integrity and the most comparable internal fabric, verified by pre-test CT screening, were selected for quantitative analysis. The discussion below therefore focuses on the representative dataset, as summarized in Table 3.

3.1 Pressure evolution and breakdown behavior

The injection pressure was continuously monitored throughout energization, well shut-in and subsequent slickwater fracturing stage, as shown in Fig. 4. Conventional slickwater fracturing (baseline, Fig. 4(a)), shows a single pressure-build cycle, where pressure rises until fracture initiation then drops sharply. In contrast, energized pre-fracturing displays a reproducible three-stage pressure trajectory (Figs. 4(b) and 4(c)), comprising a controlled pressure build during pre-pad injection to the target bottom-hole pressure of 12 MPa, a pressure decline during well shut-in as the pre-pad fluid redistributes into the matrix, and a final pressure rise and breakdown during the main slickwater fracturing stage.

To ensure comparable equilibration across fluids, shut-in time was adjusted according to the distinctive diffusivity of each pre-pad fluid (approximately 0.5 h for gaseous/SC fluids versus 3 h for aqueous fluids) until pressure variations fell below 0.1 MPa over 10 min. Stage timing differs systematically across fluid types. Since the aqueous fluids are far less

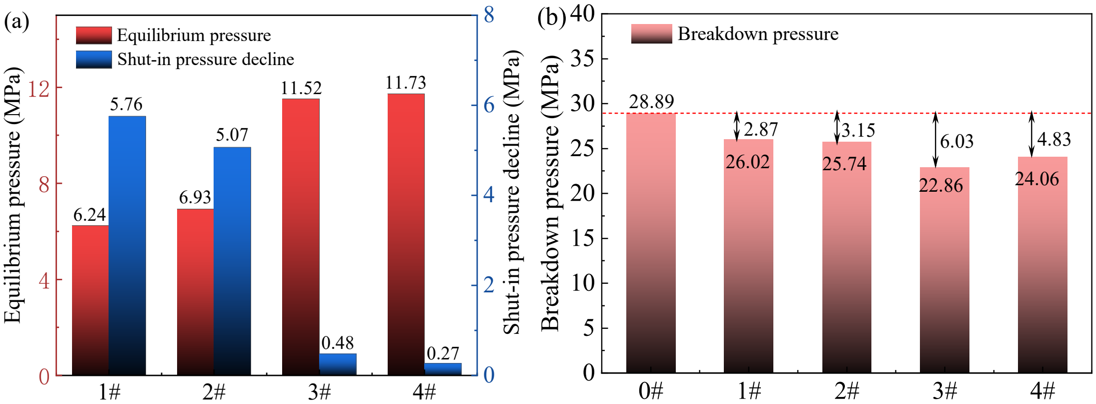

Fig. 5. Pressure response characteristics during energized pre-fracturing: (a) Pressure decline and equilibrium pressure during well shut-in; (b) breakdown pressure during the subsequent main fracturing stage.

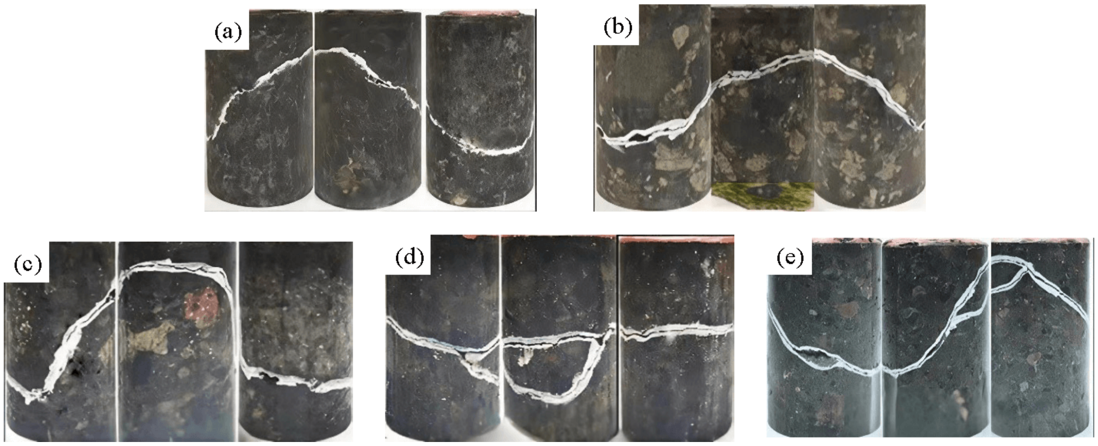

Fig. 6. Comparison of fracture surface morphology after fracturing under different pre-pad. (a) Slickwater fracturing without pre-pad; energized pre-fracturing with (b) fresh water, (c) produced water, (d) SC-CO_2, and (e) N_2.

compressible, they reach the target energization pressure more quickly than gaseous fluids. During the well shut-in, however, gaseous/SC fluids (N_2 and SC-CO_2) equilibrate substantially faster, consistent with their higher diffusivity. By comparison, the baseline slickwater-only case requires a much longer pressure build prior to breakdown because the initial matrix pressure remains low.

A key distinction emerges from shut-in pressure retention (Fig. 5(a)). Gaseous/SC pre-pads maintain significantly higher equilibrium pressures (SC-CO_2: 11.52 MPa and N_2: 11.73 MPa) than aqueous pre-pads (fresh water: 6.24 MPa and produced water: 6.93 MPa), corresponding to pressure drops of only 0.48 and 0.27 MPa for SC-CO_2 and N_2, versus 5.76 MPa and 5.07 MPa for fresh and produced water, respectively. This behavior is consistent with their greater compressibility and elastic energy storage capacity of gaseous/SC systems (Tang et al., 2024). Within each category, the slightly higher retention for N_2 than SC-CO_2 and for produced water than fresh water likely reflects subtle differences in compressibility and salinity.

As a direct consequence of elevated pore pressure before the main fracturing stage, energized pre-fracturing markedly reduces breakdown pressure relative to slickwater-only fracturing, as shown in Fig. 5(b). The reduction is more pronounced for gaseous/SC pre-pads (SC-CO_2: 6.03 MPa, 20.87%; N_2: 4.83 MPa, 16.72%) than for aqueous pre-pads (fresh water: 2.87 MPa, 9.93%; produced water: 3.15 MPa, 10.90%). Mechanistically, higher equilibrium pore pressure lowers effective stress and therefore facilitates rock failure. Notably, SC-CO_2 achieves a lower breakdown pressure than N_2 despite comparable equilibrium pressure, suggesting that physicochemical interactions may contribute additional rock weakening beyond purely poroelastic effects (Osif, 1988).

3.2 Fracture morphology characterization

To link pressure response to fracture development, fracture geometry was examined both at the specimen surface and within the interior using CT-based reconstruction. Fig. 6 compares the post-fracture surface traces (outlined in white), whereas Fig. 7 shows the 3D fracture networks reconstructed in AVIZO using watershed-based segmentation. The resulting spatial patterns were then analyzed comparatively across treatments.

Both surface inspection and CT reconstruction indicate that slickwater-only fracturing and aqueous pre-pad treatments predominantly generate a simple, planar fracture that initiates near the open-hole section and propagates in a dominant

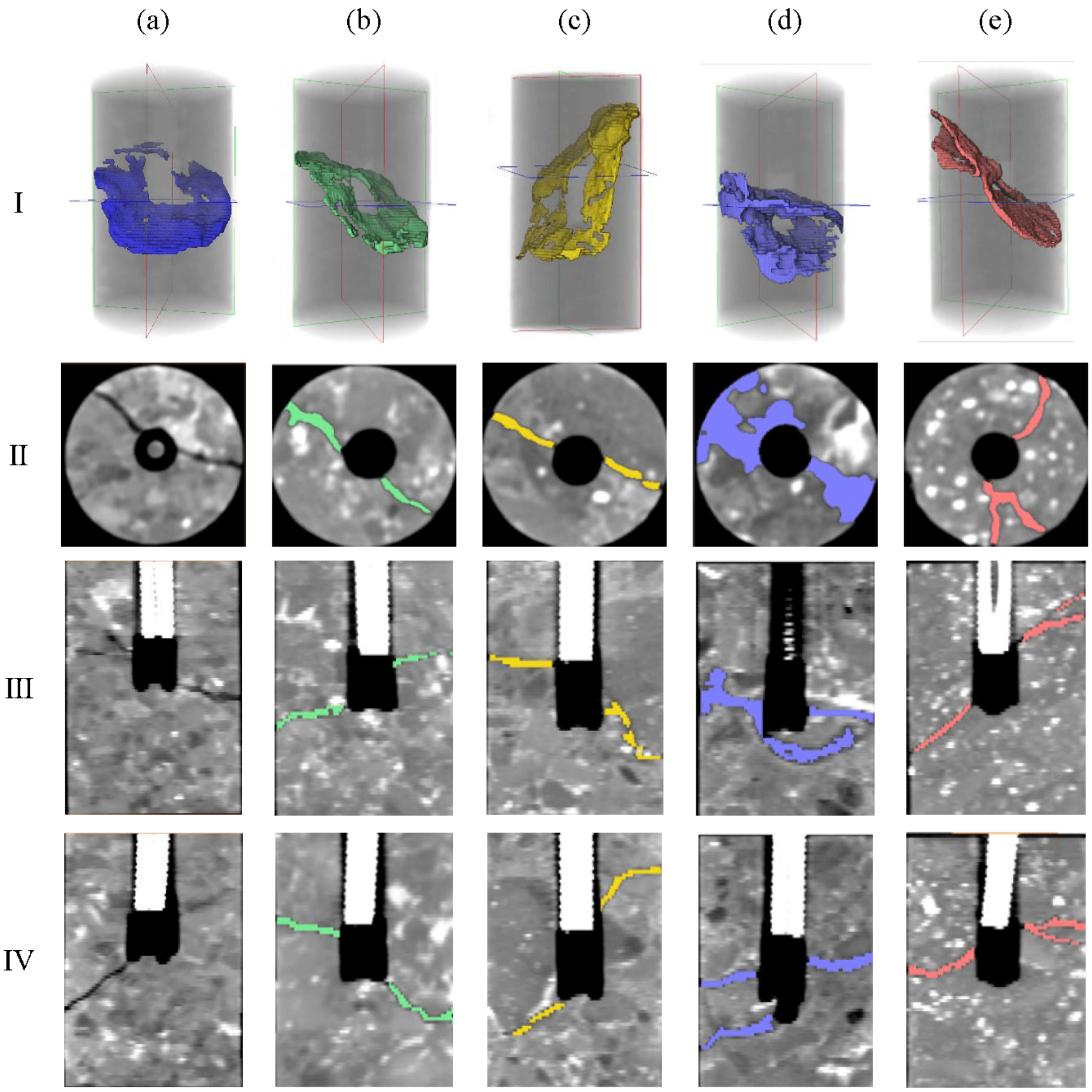

Fig. 7. 3D reconstruction of internal fracture networks obtained from X-ray CT scanning: (a) Slickwater fracturing without pre-pad; pre-fracturing with (b) fresh water, (c) produced water, (d) SC-CO_2, and (e) N_2 (I: 3D view, II: Radial slice, III and IV: Perpendicular axial slices).

direction (Fig. 6 and Figs. 7(a)-7(c)). In contrast, gaseous/SC pre-pads (SC-CO_2 and N_2) promote multi-branch fracture networks with pronounced tortuosity and spatial complexity (Fig. 6 and Figs. 7(d) and 7(e)). A notable feature in the SC-CO_2 case is that some branches initiate farther from the wellbore, which is consistent with deeper penetration and broader pressure communication during energization. These observations collectively indicate that the energization stage not only elevates pore pressure but also conditions the rock fabric in a manner that favors distributed failure and branching.

The divergence in fracture morphology can be interpreted in terms of fundamental fluid properties, particularly viscosity and interfacial tension, which govern the extent and uniformity of pore-scale penetration. Aqueous fluids, owing to higher viscosity and finite interfacial tension, preferentially advance through relatively larger pore channels, producing localized pressurization and therefore a simpler fracture geometry (conceptualized in Fig. 8). By contrast, gaseous/SC pre-pad fluids combine lower viscosity with negligible interfacial tension, enabling deeper access to micro-pore networks and creating a more spatially uniform pressure front that activates weak planes and grain boundaries, thereby promoting fracture branching (Fan et al., 2020).

3.3 Quantitative fracture complexity analysis

To corroborate the qualitative observations, fracture complexity was quantified using the FD and AR following Section 2.4, as depicted in Fig. 9. All energized pre-fracturing treatments yield higher D_f and R_a than the slickwater-only baseline ($D_f = 1.86$, $R_a = 2.04$), confirming that pre-pad energization promotes more complex fracture development.

Gaseous/SC pre-pad fluids outperform aqueous fluids in terms of fracture surface development and spatial complexity (average $R_a = 3.11$ vs. 2.41). Among all cases, SC-CO_2 produces the highest complexity ($D_f = 2.20$, $R_a = 3.34$), followed by N_2 ($D_f = 2.11$, $R_a = 2.87$). Within the aqueous group, pr-

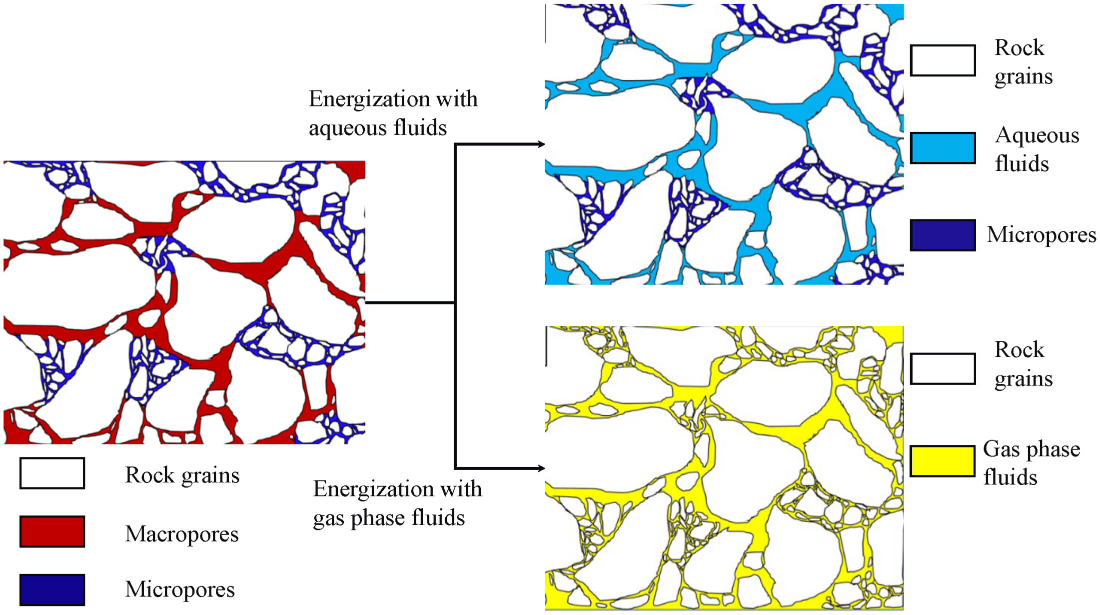

Fig. 8. Conceptual illustration of the pore-scale penetration during energized pre-fracturing with aqueous and gaseous pre-pad fluid.

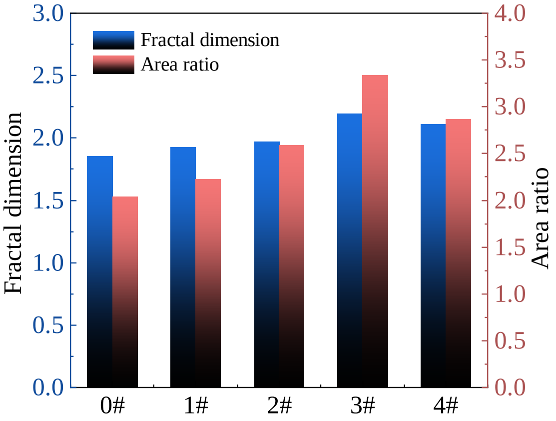

Fig. 9. Quantitative comparison of fracture complexity parameters of FD and AR for different pre-fracturing fluids.

oduced water generates slightly higher D_f and R_a ($D_f = 1.97$, $R_a = 2.59$) than fresh water ($D_f = 1.93$, $R_a = 2.23$). These metrics quantitatively confirm that SC-CO_2 energized pre-fracturing is most effective in creating complex fracture networks, whereas aqueous pre-pad treatments produce intermediate complexity, which is higher than slickwater-only but lower than gaseous/SC systems.

3.4 Pore structure of the tight conglomerate

Since pore-scale accessibility controls fluid penetration and oil mobilization, pore-throat radius conversion was established by correlating NMR T_2 distributions with MIP data from sister plugs, as shown in Fig. 10(a), following a previous study (Qu et al., 2024).

Regression in double-logarithmic coordinates yields a strong correlation ($R^2 = 0.94$) between relaxation time and pore-throat radius:

$$\lg r_c = 0.86 \lg T_2 - 1.71 \tag{14}$$

$$r_c = 0.0195 {T_2}^{0.86} \tag{15}$$

Eq. (15) enables conversion of T_2 spectra into pore-throat radius distributions. The converted NMR-derived distribution agrees closely with direct MIP measurements, as presented in Fig. 11, supporting the reliability of the calibration. Using standard pore classification (Loucks et al., 2012; Blunt et al., 2025), pores were categorized by T_2 into micropores (≤ 1 ms), mesopores (1-100 ms), and macropores ($\geq$ 100 ms), corresponding to pore-throat radii of $\leq$ 0.0195 μm, 0.0195-1.0085 μm, and $\geq$ 1.0085 μm, respectively.

The studied tight conglomerates exhibit a pore system dominated by mesopores (56.38%-60.40% of total pore volume), followed by micropores (30.44%-39.63%), whereas macropores contribute only 2.72%-6.40% (Table 4 and Fig. 12). This distribution indicates that mesopores and micropores provide the primary storage space for oil, implying that successful stimulation must effectively access and mobilize oil from small-to-intermediate pore systems rather than relying on macropore depletion alone.

3.5 Fluid migration and oil mobilization dynamics

The interaction between fracture networks and pore structure ultimately controls oil recovery. NMR was therefore used to track oil saturation evolution at three key stages, including initial oil-saturated state, post-fracturing and post-imbibition, as shown in Fig. 13. All samples initially exhibit a bimodal T_2 distribution. After treatment, the dominant signal reduction occurs in the left peak (micropores/mesopores), indicating that these pore classes contribute most to oil mobilization. Meanwhile, modest increases in the mesopore/macropore signal in

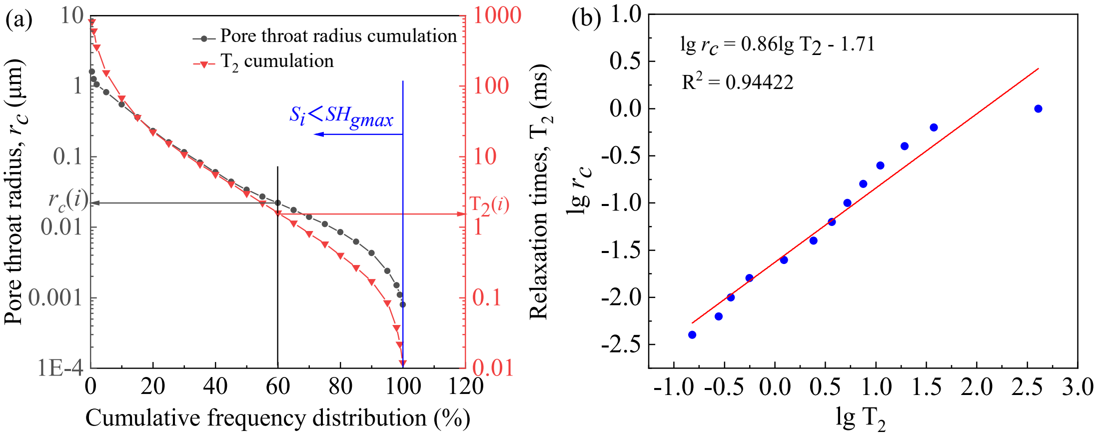

Fig. 10. Calibration of pore-throat radius during integrated NMR and MIP data: (a) Cumulative pore volume derived from NMR T_2 and MIP measurements and (b) linear regression fitting of rc and T_2.

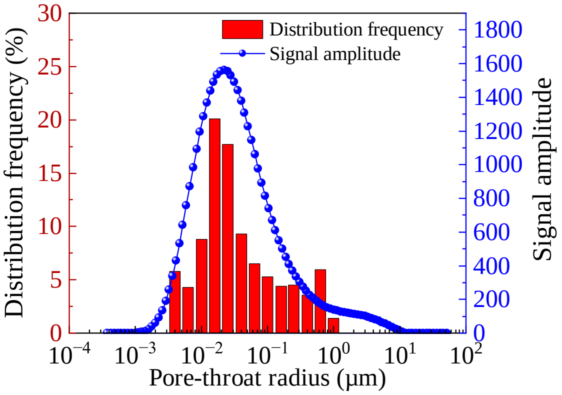

Fig. 11. Comparison of pore-throat radius distributions obtained from T_2-based conversion and direct MIP measurements.

Table 4. Pore classification in the tight conglomerates.

Pore type	T_2 (ms)	Pore radius (μm)	Proportion of pore volume (%)
Micropores	≤ 1	≤ 0.0195	30.44-39.63
Mesopores	1-100	0.0195-1.0085	56.38-60.40
Macropores	≥ 100	≥ 1.0085	2.72-6.40

some cases suggest pore-structure alteration, plausibly reflecting the development of intergranular connections that improve pore-throat connectivity and facilitate subsequent drainage into fractures.

Among the tested systems, SC-CO_2 energized pre-fracturing mobilizes oil from mesopores and micropores more effectively than the other pre-pad fluids, as evidenced by the more pronounced left-peak reduction (Fig. 13(c) with Figs. 13(a), 13(b) and 13(d)). Moreover, the T_2 spectrum evolves toward a trimodal distribution after imbibition in the SC-CO_2-formation water system, implying a redistribution of pore-size-associated signals rather than a simple uniform depletion.

This behavior is consistent with geochemical interactions during the well shut-in in the presence of SC-CO_2 and formation water. Mineral dissolution (e.g., calcite), supported by parallel XRD results showing a decrease from 32.6% to 21.3%, can enlarge existing micropores into mesopores while also generating secondary microporosity. Consistently, MIP measurements indicate a 78.49% increase in average pore-throat radius, suggesting improved petrophysical properties and connectivity (Kaszuba et al., 2003; Soleiman Asl et al., 2022). The splitting of the original left peak into two sub-peaks therefore provides a pore-scale signature of dynamic pore-structure modification, which enhances imbibition efficiency and subsequent oil transport (Gunter et al., 1997; Rathnaweera et al., 2016). Together, these effects indicate that SC-CO_2 energized pre-fracturing couples mechanical stimulation with chemically assisted pore accessibility, thereby maximizing recovery potential.

3.6 Effects of energized pre-pad fluid on ultimate oil recovery

Ultimate oil recovery reflects the combined effects of fracture network complexity and pore-scale mobilization. Oil recovery ratios and pore-size-specific contributions derived from NMR T_2 analyses are summarized in Table 5 and Fig. 14. Across both post-fracturing and post-imbibition stages, gaseous/SC pre-pad fluids consistently achieve higher recovery than aqueous systems.

SC-CO_2 energized pre-fracturing yields the highest recovery after imbibition (36.67%), followed by N_2-formation water (32.77%), produced water (27.31%) and fresh water (26.81%), as shown in Fig. 14(a). The 9.86% improvement of SC-CO_2 over fresh water can be decomposed into two coupled components: Enhanced fracture complexity, which increases post-fracturing recovery by 6.85%, and chemically driven pore-structure modification during imbibition, which contributes an additional 3.01%. Produced water exhibits marginally higher recovery than fresh water, potentially reflecting the presence of surface-active components, although their key physical properties and fracture patterns are broadly comparable. Absolute oil recovery follows the same ranking with reduced magnitude (Fig. 14(b)).

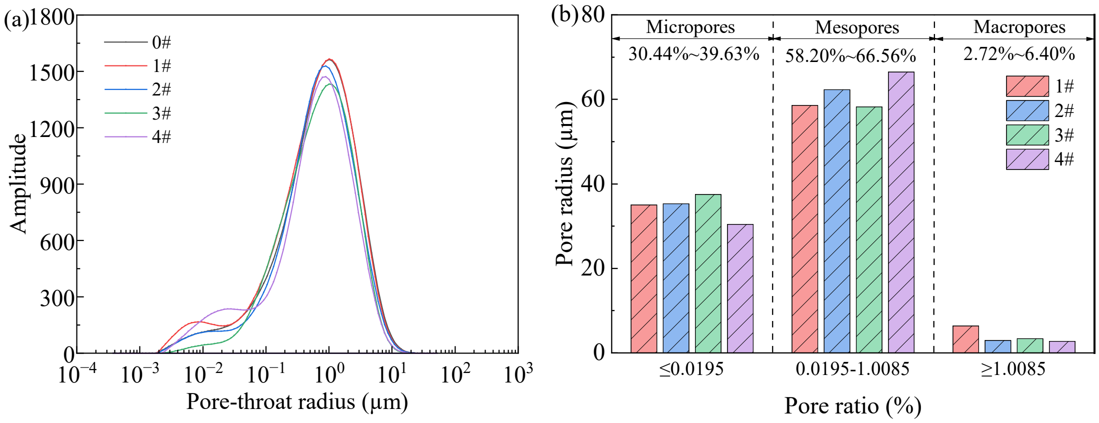

Fig. 12. Pore structure characteristics of tight conglomerate samples: (a) NMR T_2 spectra and (b) pore-throat radius distribution and corresponding volumetric proportions.

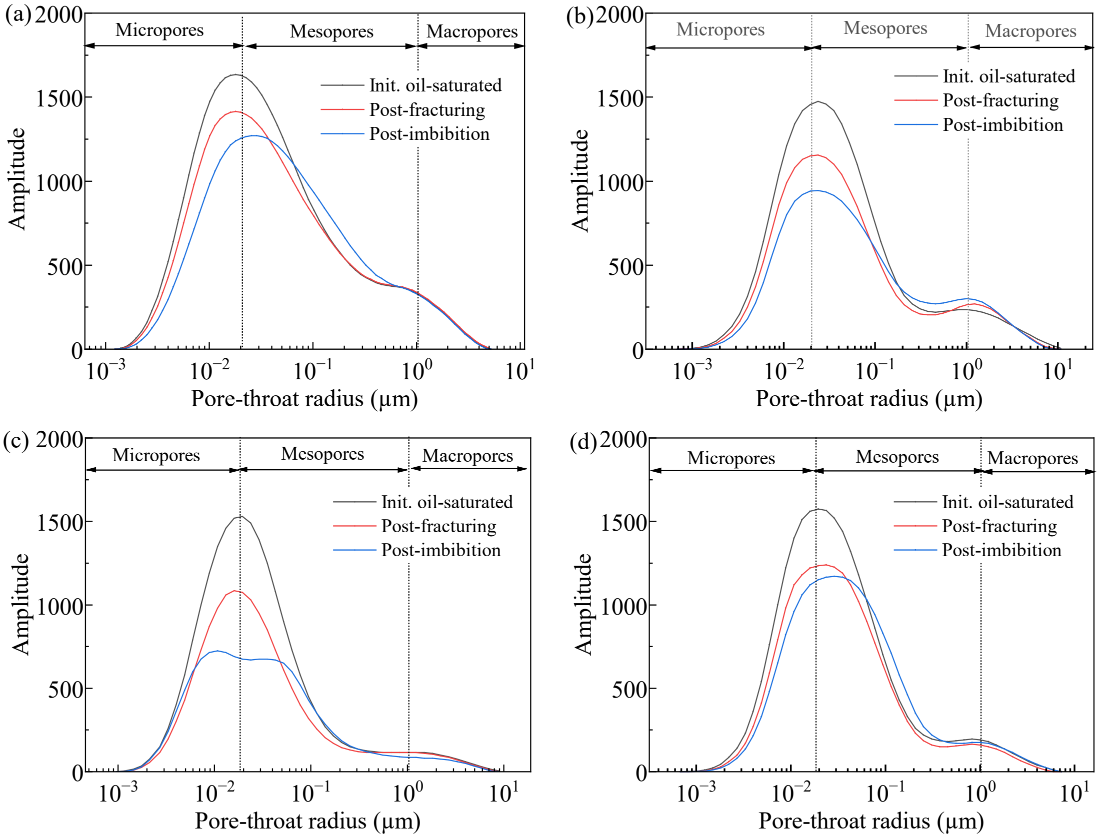

Fig. 13. Evolution of NMR T_2 spectra at different stages for pre-fracturing with aqueous/gaseous pre-pad fluids: (a) Fresh water, (b) produced water; (c) SC-CO_2-formation water and (d) N_2-formation water.

Pore-scale contribution analysis further reveals that over 94% of the imbibition-associated recovery originates from micropores and mesopores (Figs. 14(c) and 14(d)). After fracturing, mesopores contribute 52.47%-61.59% of recovered oil, exceeding the micropore contribution (35.02%-46.45%), which is consistent with preferential drainage from more accessible pore classes once fractures provide connected pathways. During imbibition, the contribution from micropores increases for aqueous systems (48.25%-49.88%), approaching that of mesopores (50%-55%), indicating continued mobilization from the smaller pores during shut-in.

The SC-CO_2-formation water system exhibits a distinct inversion. The contribution from micropores decreases from 46.45% (post-fracturing) to 38.83% (post-imbibition), whereas the mesopore contribution increases. This shift aligns with the dissolution-driven enlargement of micropores into mesopores during imbibition, which dynamically alters the pore-size distribution and transfers the dominant contribution from micropores to mesopores.

Table 5. Oil recovery performance and pore-scale contributions for energized pre-fracturing with aqueous and gaseous pre-pad fluids.

Pre-pads	Oil recovery ratio (%)		Contribution of different pore sizes (%)					
	Post-fracturing	Post-imbibition	Post-fracturing			Post-imbibition		
			Micropores	Mesopores	Macropores	Micropores	Mesopores	Macropores
Fresh water	20.24	26.81	35.02	61.59	3.39	48.93	49.85	1.21
Produced water	22.16	27.31	36.80	57.54	5.66	49.88	52.25	-2.13
SC-CO_2	27.09	36.67	46.45	52.47	1.08	38.83	57.17	3.99
N_2	23.54	32.77	40.52	60.85	-1.37	48.25	55.23	-3.48

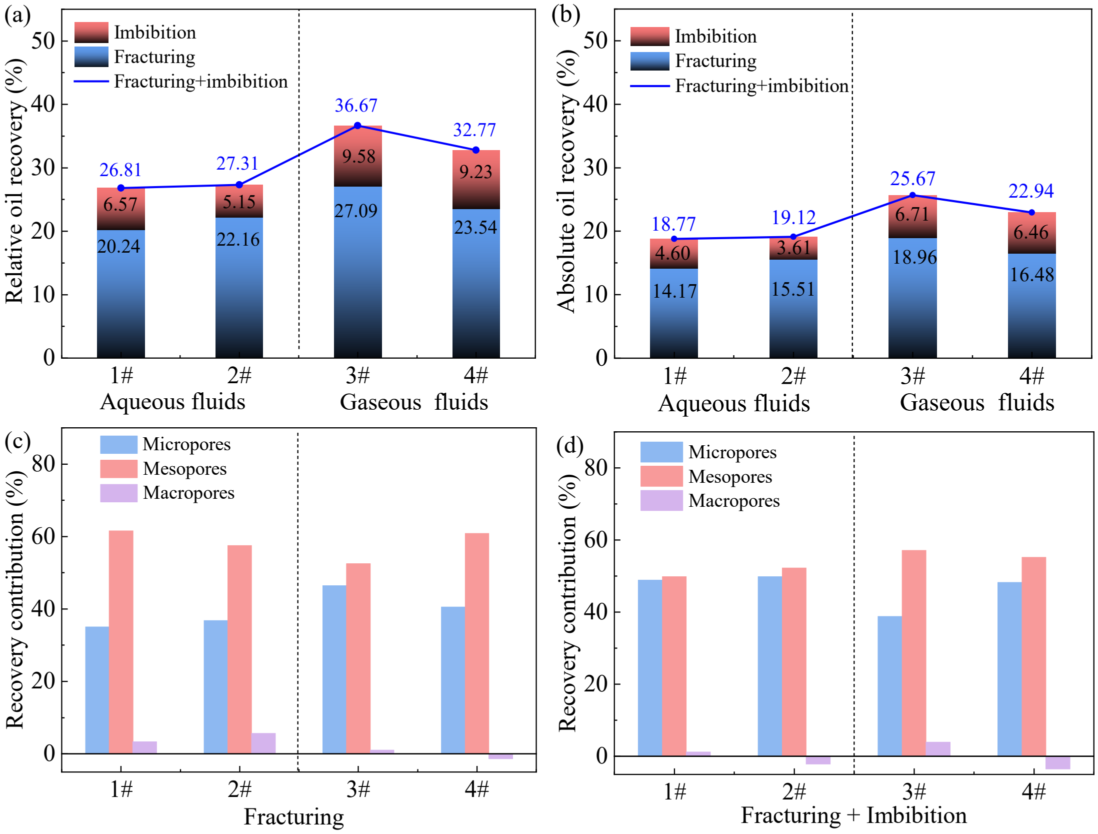

Fig. 14. Oil recovery characteristics under different energized pre-fracturing treatments: (a) Relative oil recovery at different stages, (b) absolute oil recovery, pore scale contributions (c) after fracturing and (d) after fracturing and imbibition.

4. Conclusions

This study establishes an integrated experimental framework to elucidate the coupled mechanisms of fracture propagation and imbibition-driven oil recovery during energized pre-fracturing in tight conglomerate reservoirs. By integrating CT-based fracture characterization with NMR-based fluid saturation monitoring, the performance of aqueous (fresh/produced water) and gaseous (SC-CO_2/N_2) pre-pad fluids was systematically evaluated. The main conclusions are summarized as follows:

1) Energized pre-fracturing effectively reduces breakdown pressure in tight conglomerates compared with conventional slickwater fracturing, with gaseous pre-pad fluids exhibiting a more pronounced reduction (16.72%-20.87%) than aqueous fluids (9.93%-10.90%), owing to superior pressure retention and energy storage capacity.
2) Gaseous pre-pad fluids promote substantially higher fracture complexity than aqueous fluids, which in turn is higher than that by slickwater-only fracturing. In particular, SC-CO_2 produces the most intricate, multi-branch fracture networks, highlighting its strong capability to activate weak planes and enhance fracture connectivity.
3) Mesopores and micropores dominate the pore system and control oil storage in tight conglomerate. The pore

structure is primarily composed of mesopores (up to 60.40%) and micropores (up to 39.63%), which together constitute the main oil storage space and therefore exert a controlling influence on initial oil distribution as well as subsequent oil mobilization and recovery.

4) Enhanced fracture complexity and pore-scale mobilization jointly improve oil recovery. Both post-fracturing and post-imbibition oil recovery are consistently higher for gaseous pre-pad fluids than for aqueous fluids. More than 94% of the recovered oil originates from mesopores and micropores, with the contribution from micropores increasing during imbibition, reflecting progressive oil mobilization from smaller pore systems during shut-in.

Acknowledgements

This work is supported by the National Natural Science Foundation of China (No. 52174044), Science and Technology Department of Xinjiang Uyghur Autonomous Region (No. 2024B01013-1), Tianshan Talent Training Program (No. T2024TSYCCX0070) and Xinjiang Uygur Region “One Case, One Policy” Strategic Talent Introduction Project (No. XQZX20240054).

Conflicts of interest

The authors declare no competing interest.

References

Abragam, A. The principles of nuclear magnetism. Oxford, UK, Oxford University Press, 1961.

Alharthy, N. S., Teklu, T. W., Kazemi, H., et al. Flow dynamics of CO_2 and propane injection into tight oil reservoirs. Journal of Petroleum Science and Engineering, 2018, 166: 301-313.

Ampomah, W., Balch, R. S., Cather, M., et al. Optimum design of CO_2 storage and oil recovery under geological uncertainty. Applied Energy, 2017, 195: 80-92.

Bahrami, H., Rezaee, R., Clennell, B. Water blocking damage in hydraulically fractured tight sand gas reservoirs: An example from Perth Basin, Western Australia. Journal of Petroleum Science and Engineering, 2012, 88-89: 100-106.

Bennion, D. B., Bachu, S. Drainage and imbibition relative permeability relationships for supercritical CO_2/brine and H2S/brine systems in intergranular sandstone, carbonate, shale, and anhydrite rocks. SPE Reservoir Evaluation & Engineering, 2008, 11(3): 487-496.

Blunt, M. J., Sun, S., Boone, M. A., et al. Digital rock physics and fluid flow in the context of the energy transition. Advances in Geo-Energy Research, 2025, 18(3): 299-302.

Brown, R. J. S., Fatt, I. Measurements of fractional wettability of oil fields’ rocks by the nuclear magnetic relaxation method. Paper SPE 743-G Presented at the Petroleum Branch Fall Meeting, Los Angeles, California, 14-17 October, 1956.

Cipolla, C. L., Warpinski, N. R., Mayerhofer, M. J., et al. The relationship between fracture complexity, reservoir properties, and fracture treatment design. SPE Production & Operations, 2010, 25(4): 438-452.

Clarke, R. H. Reservoir properties of conglomerates and conglomeratic sandstones: Geologic notes. AAPG Bulletin, 1979, 63(5): 799-803.

Coates, G. R., Xiao, L., Prammer, M. G. NMR Logging Principles and Applications. Houston, USA, Halliburton Energy Services, 1999.

Dai, H., Yin, T., Wu, Y., et al. Characterization of fracture extension and damage evolution in hot dry rock by cycle hydraulic fracturing (CHF): Application of CHF in enhanced geothermal systems. Energy, 2025, 330: 137007.

Elgibaly, A. A., Salem, A. M., Soliman, Y. A. Improving hydraulic fracturing effectiveness in depleted and low-pressure reservoirs using N_2-energized fluids. Journal of Petroleum Exploration and Production Technology, 2021, 11(2): 857-873.

Fan, L., Li, L., Su, Y., et al. CO_2-prepad injection EOR simulation and sensitivity analysis considering miscibility and geomechanics in tight oil reservoirs. Journal of Petroleum Science and Engineering, 2020, 195: 107905.

Fang, Z., Hao, W., Nuertai, M., et al. Characteristics and controlling factors of petroliferous reservoirs in the Permian Lower Urho Formation, western Mahu slope, Junggar Basin, northwest China. Interpretation, 2023, 11(4): T567-T579.

Faroughi, S. A., Pruvot, A. J. C. J., McAndrew, J. The rheological behavior of energized fluids and foams with application to hydraulic fracturing: A review. Journal of Petroleum Science and Engineering, 2018, 163: 243-263.

Goral, J., Panja, P., Deo, M., et al. Confinement effect on porosity and permeability of shales. Scientific Reports, 2020, 10(1): 14770.

Gunter, W. D., Gentzis, T., Rottenfusser, B. A., et al. Deep coalbed methane in Alberta, Canada: A fuel resource with the potential of zero greenhouse gas emissions. Energy Conversion and Management, 1997, 38: S217-S222.

Hamida, T., Babadagli, T. Immiscible displacement of oil by water in consolidated porous media due to capillary imbibition under ultrasonic waves. The Journal of the Acoustical Society of America, 2007, 122(3): 1539-1555.

Holditch, S. A. Factors affecting water blocking and gas flow from hydraulically fractured gas wells. Journal of Petroleum Technology, 1979, 31(12): 1515-1524.

Hosseini, M., Ali, M., Fahimpour, J., et al. Energy storage in carbonate and basalt reservoirs: Investigating secondary imbibition in H_2 and CO_2 systems. Advances in Geo-Energy Research, 2024, 11(2): 132-140.

Hubbert, M. K., Willis, D. G. Mechanics of hydraulic fracturing. Transactions of the AIME, 1957, 210: 153-168.

Huang, Z., Zhang, S., Yang, R., et al. A review of liquid nitrogen fracturing technology. Fuel, 2020, 266: 116067.

Ishida, T., Aoyagi, K., Niwa, T., et al. Acoustic emission monitoring of hydraulic fracturing laboratory experiment with supercritical and liquid CO_2. Geophysical Research Letters, 2012, 39(16): L16309.

Kaszuba, J. P., Janecky, D. R., Snow, M. G. Carbon dioxide reaction processes in a model brine aquifer at 200 °C and 200 bars: Implications for geologic sequestration of carbon. Applied Geochemistry, 2003, 18(7): 1065-1080.

Kamali, A., Ghassemi, A. Impact of rock heterogeneity on hydraulic fracture propagation and fracture network complexity. Geomechanics for Energy and the Environment, 2022, 30: 100285.

Kozhevnikov, E., Turbakov, M., Riabokon, E., et al. The mechanism of porous reservoir permeability deterioration due to pore pressure decrease. Advances in Geo-Energy Research, 2024, 13(1): 96-105.

Lei, Q., Weng, D., Guan, B., et al. A novel approach of tight oil reservoirs stimulation based on fracture controlling optimization and design. Petroleum Exploration and Development, 2020, 47(3): 632-641.

Li, R., Zhai, H., Jiang, C., et al. A review of laboratory hydraulic fracturing experiments on shales. Geoenergy Science and Engineering, 2025, 254: 214028.

Loucks, R. G., Reed, R. M., Ruppel, S. C., et al. Spectrum of pore types and networks in mudrocks and a descriptive classification for matrix-related mudrock pores. AAPG Bulletin, 2012, 96(6): 1071-1098.

Mandelbrot, B. B. The Fractal Geometry of Nature. San Francisco, USA, W. H. Freeman, 1982.

Middleton, R. S., Carey, J. W., Currier, R. P., et al. Shale gas and non-aqueous fracturing fluids: Opportunities and challenges for supercritical CO_2. Applied Energy, 2015, 147: 500-509.

Mojid, M. R., Negash, B. M., Abdulelah, H., et al. A state-of-the-art review on waterless gas shale fracturing technologies. Journal of Petroleum Science and Engineering, 2021, 196: 107976.

Morrow, N. R., Mason, G. Recovery of oil by spontaneous imbibition. Current Opinion in Colloid & Interface Science, 2001, 6(4): 321-337.

Nelson, P. H. Pore-throat sizes in sandstones, tight sandstones, and shales. AAPG Bulletin, 2009, 93(3): 329-340.

Osif, T. L. The effects of salt, gas, temperature, and pressure on the compressibility of water. SPE Reservoir Engineering, 1988, 3(1): 175-181.

Peng, S., Liu, Y., Ko, L. T., et al. Water/oil displacement by spontaneous imbibition through multiscale imaging and implication on wettability in Wolfcamp shale. Paper URTeC 2019-194 Presented at the 7th Unconventional Resources Technology Conference, Denver, Colorado, 22-24 July, 2019.

Perera, M. S. A., Ranjith, P. G., Airey, D. W., et al. Sub- and super-critical carbon dioxide flow behavior in naturally fractured black coal: An experimental study. Fuel, 2011, 90(11): 3390-3397.

Qin, L., Zhang, X., Zhai, C., et al. Advances in liquid nitrogen fracturing for unconventional oil and gas development: A review. Energy & Fuels, 2022, 36(6): 2971-2992.

Qu, H., Peng, Y., Huang, J., et al. Modelling of the impact of stress concentration on permeability in porous medium based on machine learning method. Geoenergy Science and Engineering, 2023a, 224: 211655.

Qu, H., Peng, Y., Pan, Z., et al. Numerical study on the impact of water-rock interactions on the propagation of water-flooding induced fracture. Frontiers in Earth Science, 2023b, 11: 1129913.

Qu, H., Shi, J., Wu, M., et al. Experimental study on the mechanism of enhanced imbibition with different types of surfactants in low-permeability glutenite reservoirs. Molecules, 2024, 29(24): 5953.

Qu, H., Zhang, J., Zhou, F., et al. Evaluation of hydraulic fracturing of horizontal wells in tight reservoirs based on the deep neural network with physical constraints. Petroleum Science, 2023c, 20(2): 1129-1141.

Rathnaweera, T. D., Ranjith, P. G., Perera, M. S. A., et al. Experimental investigation of geochemical and geomechanical changes in saline aquifer-caprock system during sequestration of supercritical CO_2. International Journal of Greenhouse Gas Control, 2016, 50: 103-117.

Rodriguez, A. Z., Wang, H., Hu, L., et al. Treatment of produced water in the Permian Basin for hydraulic fracturing: Comparison of different coagulation processes and innovative filter media. Water, 2020, 12(3): 795.

Saidian, M., Prasad, M. Effect of mineralogy and clay content on wettability of unconventional reservoir rocks using NMR relaxation history. Journal of Petroleum Science and Engineering, 2015, 133: 742-753.

Soleiman Asl, T., Habibi, A., Yassin, M. R., et al. An experimental and field case study to evaluate the effects of shut-in on well performance. Journal of Petroleum Science and Engineering, 2022, 208: 109318.

Sondergeld, C. H., Newsham, K. E., Comisky, J. T., et al. Petrophysical characterization of shale reservoirs. Paper SPE 131768 Presented at the SPE Unconventional Gas Conference, Pittsburgh, Pennsylvania, 23-25 February, 2010.

Soomro, N. A., Ansari, U., Shams, B., et al. Experimental assessment of the stability and impact of water-based fracturing fluid with and without triethanolamine (TEA). Fuel Communications, 2025, 23: 100137.

Sun, X. Z., Zhang, J. C., Han, F. P., et al. Investigation into the stimulation effect of energized fracturing: An experimental study. Paper ARMA-2025-0521 Presented at the 59th U.S. Rock Mechanics/Geomechanics Symposium, Santa Fe, New Mexico, USA, 8-11 June, 2025.

Tang, W., Zhou, F., Zheng, X., et al. Evaluation of matrix energization effect of pre-fracturing method in tight reservoirs- a comparative study of CO_2, N_2, and water. Geoenergy Science and Engineering, 2024, 233: 212535.

Tang, W., Zhou, F., Sheng, J. J., et al. Further investigation of CO_2 energization fracturing in shale reservoir-from microscopic mechanism to field application. Fuel, 2025, 385: 134156.

Vogel, H. J., Kretzschmar, A. Topological characterization of pore space in soil-sample preparation and digital image processing. Geoderma, 1996, 73(1-2): 23-38.

Wang, L., Du, Y., Wu, G., et al. Application of nuclear magnetic resonance technology in reservoir characterization and CO_2 enhanced recovery for shale oil: A review. Marine and Petroleum Geology, 2025, 177: 107353.

Warpinski, N. R., Mayerhofer, M. J., Vincent, M. C., et al. Stimulating unconventional reservoirs: Maximizing network growth while optimizing fracture conductivity. Journal of Canadian Petroleum Technology, 2009, 48(10): 39-51.

Xie, H. Fractals in Rock Mechanics. Rotterdam, Netherlands, A. A. Balkema, 1993.

Xie, Z., Huang, Z., Sun, Z., et al. The interaction behaviors between the hydraulic fracture and natural fracture in hot dry rock. Geoenergy Science and Engineering, 2025, 247: 213731.

Xu, X., Wan, Y., Li, X., et al. Microscopic imbibition characterization of sandstone reservoirs and theoretical model optimization. Scientific Reports, 2021, 11(1): 8509.

Yu, J., Li, N., Hui, B., et al. Experimental simulation of fracture propagation and extension in hydraulic fracturing: A state-of-the-art review. Fuel, 2024, 363: 128229.

Zhang, X., Song, X., Li, X., et al. Supercritical CO_2 injection-induced fracturing in Longmaxi shales: A laboratory study. Energies, 2025, 18(2): 855.

Zhang, Y., Chang, J., Jiang, Z., et al. Visualization of dynamic micro-migration of shale oil and investigation of shale oil movability by NMRi combined oil charging/water flooding experiments: A novel approach. Marine and Petroleum Geology, 2024, 165: 106907.

Zhao, Y., Li, X., Wang, M., et al. Quantitative characterization of soil micropore structure and pore water content using nuclear magnetic resonance: Challenges and calibration methods. Frontiers of Structural and Civil Engineering, 2025, 19(1): 76-92.